

Microscopy of diffuse nematic-isotropic transition in main-chain nematic liquid crystal elastomers

Takuya Ohzono^{1}, Kaoru Katoh², Eugene M. Terentjev³*

¹ Research Institute for Electronics and Photonics, National Institute of Advanced Industrial Science and Technology (AIST), 1-1-1 Higashi, Tsukuba 305-8565, Japan

² Biomedical Research Institute, AIST, 1-1-1 Higashi, Tsukuba 305-8566, Japan.

³ Cavendish Laboratory, University of Cambridge, J.J. Thomson Avenue, Cambridge, CB3 0HE, United Kingdom

ABSTRACT: Nematic-isotropic phase transition in liquid crystal elastomers (LCE), which drastically alters the macroscopic properties of the material, is attractive for both fundamental physics and applications. Here, we introduce new experimental methods based on polarized and fluorescence optical microscopy to characterize the phase transition of polydomain LCE, monitoring the order parameter and the nematic domain structure. It is demonstrated that polydomain main-chain nematic LCE exhibit an ordering transition very different from the classical first-order one, having a diffuse continuous nature. Unexpectedly, characteristic correlation length of the fading polydomain structure remains unchanged across the transition.

Introduction

One of the important properties of nematic liquid crystal elastomers (LCE)¹ is the nature of their nematic-isotropic (N-I) phase transition. Since this transition induces drastic changes in macroscopic shape and viscoelastic properties, LCE have shown potential as artificial muscles,²⁻⁴ morphing and shape-memory materials⁵, dynamic tribological materials for controlling adhesion⁶⁻⁸ and friction,^{9,10} and dynamic optical elements.¹¹ Thus, understanding of the transition nature is important to optimize the material responses triggered by the N-I transition for various applications.

In the conventional liquid crystals¹² the N-I transition is strictly first order due to the underlying quadrupolar symmetry of the emerging phase, with the discontinuity in the orientational order parameter Q at the thermodynamically equilibrium transition point. In contrast, several experiments in LCE¹³⁻¹⁹ show a smooth, continuous transition as a function of temperature, T . Some qualitative explanations for this smooth (continuous) transition have been proposed by extending the phenomenological Landau-de-Gennes model. The first such explanation starts with the original de Gennes work on strain-nematic coupling for the LCE under external uniaxial strain.²⁰ Indeed, the linear coupling of the tensor nematic order parameter Q_{ij} with the imposed strain tensor would reduce the initial first order transition to a supercritical, continuous transition. The resulting state with a residual non-zero value of Q above the critical temperature T_c is often called the “paranematic state”. For polydomain LCE free from external strain, some models²¹⁻²³ considering the quenched random disorder embedded within the polymer network reproduce the diffuse transition nature similar to the supercritical behavior under external field, although the replica symmetry-breaking model²⁴

has also pointed at a possible continuous critical point. Experimentally, in the carefully prepared side-chain LCE of isotropic genesis and no chain entanglements, a continuous critical point was confirmed by NMR evaluation^{25,26} of T -dependent local order parameter Q . However, all LCE of nematic genesis invariably show a diffuse supercritical onset of the nematic order, increasingly so when additional internal constraints (such as chain entanglements) are present.

So far, in the pure polydomain LCE material, the experimental method to evaluate the local order parameter Q , which is different from the macroscopic alignment measure characterized by X-ray or birefringence, has been limited to NMR, where deuterium substitution on the polymer network is usually needed.^{1,14,25,26} Thus, more convenient methods to evaluate Q at least at the length scale of nematic polydomain, $\sim 1 \mu\text{m}$, would help studying the N-I transition nature of various LCE recently synthesized.^{7,27-30} Here, we introduce alternative techniques leveraging the conventional polarized optical microscopy (POM) and the polarized fluorescence microscopy (PFOM).³¹⁻³³ The former and latter give material birefringence and the local dichroism of fluorescent probes, respectively, both of which are closely related to the value of Q averaged locally in polydomain LCE. Moreover, since PFOM also provides real-space information on local nematic director orientation, it is possible to monitor the T -dependent domain properties, e.g., the characteristic polydomain textures^{1,34-36} and the correlation length, changing upon N-I transition. Although the inherent quenched random disorder, disturbing the long range nematic order, is assumed to be the origin of the correlation length (equilibrium domain size), the related experiment has been limited, e.g., to that in the reciprocal space by the depolarized light scattering (DPLS).^{37,38} On the recently

developed main-chain LCE based on the thiol-ene reaction,^{7,27-30} no polydomain texture has been studied yet. T -dependent microstructures resolved here are analysed together with the data on Q , and DPLS patterns. In agreement with earlier studies, the results show that the N-I transition is more diffuse on LCE, in proportion to the increasing density of effective crosslinks. Unexpectedly, we find that characteristic lengths of the polydomain on LCE remain almost constant throughout the N-I transition.

Results

LCE with different effective crosslink densities. It is well known that the conditions of the crosslinking determine the state of entanglements of network strands, which in turn represent permanent constraints since the reptation motion of chains is prevented by crosslinking.³⁹ When a network is fully crosslinked in a swollen state, on de-swelling the initially stretched polymer strands fold densely, but without permanent entanglements. In contrast, when the crosslinking is established in a melt, or at low solvent content, the probability of permanently fixing entangled configuration is increased. In [Figure 1a](#), schematics are shown for the two LCE networks with different densities of entanglements, prepared with the mass ratio of the polymer to solvent, $\Phi = 0.95$ and 0.45 upon polymerization ([Methods](#)).

In addition, the different Φ can cause difference in the polymerization degree. The lower Φ (i.e. the higher fraction of solvent) may result in the higher number of dangling ends, which also affects the effective crosslink density. Although the true effects from these two differences, degrees of entanglement and polymerization, are difficult to be quantified

separately, at least the effective crosslink density, which governs the degree of quenched network disorder, is parameterized on the present two systems ($\Phi = 0.95$ and 0.45).

The wide-angle X-ray scattering (WAXS) pattern showing a simple isotropic halo (**Figure S1**) confirms that the sample in the nematic phase is macroscopically isotropic. On the mesoscopic length scale to an observer who is unaware of polymer strands, the local nematic director \mathbf{n} can be defined, as shown in **Figure 1b**. Since the degrees of entanglements and polymerization can modulate the effective crosslink density, their effective elastic moduli μ may differ (**Figure 2**). Indeed, the higher stress at any strain, and the lower breaking strain for the sample prepared with $\Phi = 0.95$ are attributed to a mixed effect from the higher entanglement density and the higher polymerization degree. The thermal analysis shows that N-I transition temperatures, T_{NI} , are around 40 and 43°C for LCE with $\Phi = 0.95$ and 0.45 , respectively, again confirming the effect of internal constraints in the two systems. The glass transition temperatures are estimated to be less than -30°C for both materials (**Figure 1c**).

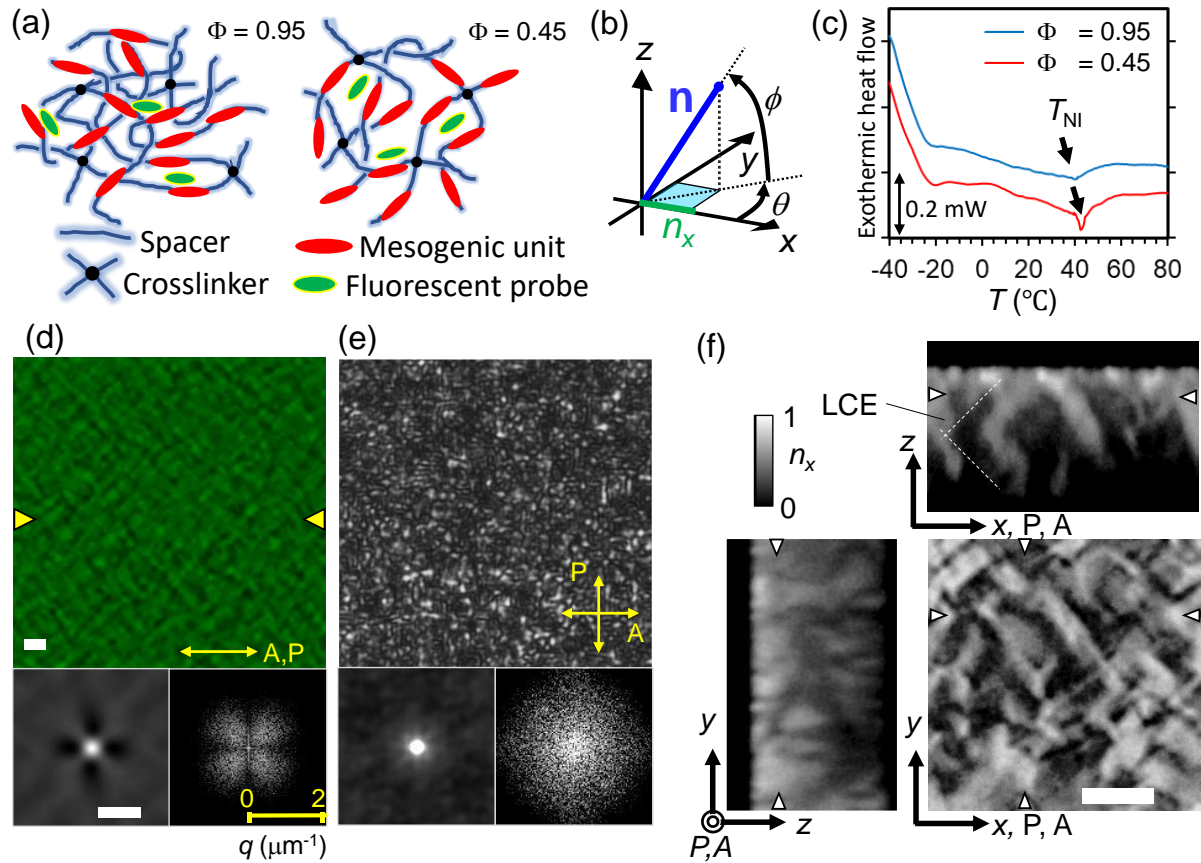


Figure. 1 Polydomain LCE. (a) Schematics for main-chain LCE network structures with different densities of entanglements prepared with the solute mass ratio $\Phi = 0.95$ and $\Phi = 0.45$ upon polymerization. Their polymerization degrees may also differ. (b) The definition of the unit nematic director in the coordinate system. The x -component, n_x , is imaged with PFOM with the polarizers in the x direction. (c) DSC curves on heating, showing N-I transition peaks around $T_{NI} = 40 \pm 1^\circ\text{C}$ or $43 \pm 1^\circ\text{C}$ on LCE with $\Phi = 0.95$ or 0.45 , respectively. (d)-(f) Typical microscopies on LCE with $\Phi = 0.95$ at $T = 20^\circ\text{C}$. (d) PFOM image with ACF (bottom-left) and FFT (bottom-right). The polarizers (A, P) are set in the horizontal, x , direction (yellow arrow). (e) POM under crossed polarizers with ACF and FFT. (f) 3D confocal PFOM image with cross-sections. White triangles indicate positions of sections. Polarizers are in the x direction. (Bars: $2 \mu\text{m}$)

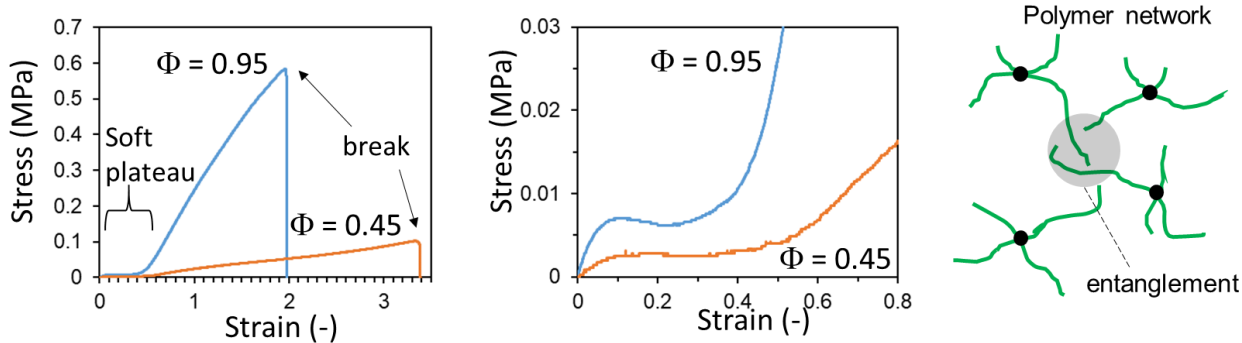


Figure. 2 Effects of solvent concentration upon polymerization on elastomer network.

Stress-strain curves to break of the polydomain LCE prepared with $\Phi = 0.95$ (lower solvent amount) and $\Phi = 0.45$ (higher solvent amount). The soft plateau region is highlighted in the middle panel. The uniaxial strain was applied at the rate of 0.001 s^{-1} to the long strip strips ($40 \text{ mm} \times 5 \text{ mm} \times \sim 0.8 \text{ mm}$) until their break at 20°C (nematic state). The curve shapes are common to the polydomain LCE, showing the soft plateau region followed by the elastic response at higher strain. The main differences are: (1) the wider soft plateau region, (2) higher strain to break, and (3) lower effective modulus for the sample with $\Phi = 0.45$. Given the identical chemical composition of the monomers, the results (2) and (3) clearly indicates that, for the sample with $\Phi = 0.95$, the average length of network strands is smaller, and thus, the higher effective crosslinking density mainly due to the entanglements (shown in the right schematic) is deduced. Strictly speaking, the possibly higher density of dangling bonds in the sample with $\Phi = 0.45$ might also contribute to this difference.

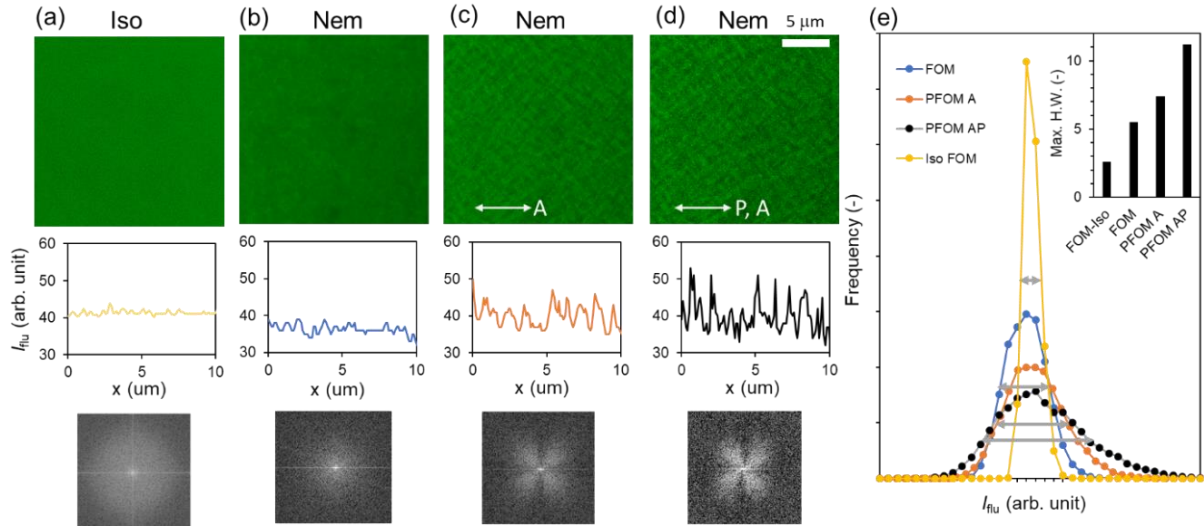


Figure 4. Effect of modes on fluorescence microscopy with the typical cross-sectional profiles and FFTs. We can consider that the maximum-half-width of the fluorescence intensity distribution obtained (a) at isotropic temperature (65°C), in which the uniform fluorescence distribution is assumed as the basal noise range of the present system. (b) On the image of the polydomain sample observed without polarizers, the non-negligible contrast should reflect the angle ϕ (out-of-plane angle of the TDM). Owing to the high NA of the lens, which can collect the fluorescence from the probes with high ϕ , the clear contrast is not expected for the difference in the angle ϕ . (c) With a polarizer as the analyser in the horizontal direction, the intensity strongly reflects the in-plane angle, θ , of the probe, i.e., the nematic director \mathbf{n} projected on the xy -plane. In this case, the contrast increases showing that the characteristic patterns with the correlation in the diagonal directions ($\pm 45^{\circ}$ from the director). (d) When another polarizer is added for the excitation light in the horizontal direction, the contrast further increases (see ref.³³ for the contrast enhancement mechanism). (e) The increase of the maximum-half-width is associated with that of the contrast.

Polydomain structures. The typical PFOM images of our polydomain LCE are shown in **Figures 1d** and **3**, and the intensity profiles are shown in **Figures 4** and **5**. **Figure 4** also

shows how the polydomain appears in each fluorescence detection modes compared to the isotropic state without the texture. Here, we used coumarin dye (**Figure S2**) as an anisotropic fluorescent probe that aligns with the local \mathbf{n} orientation. In contrast to the simple fluorescence image without polarizers, PFOM shows characteristic anisotropic patterns. Since the fluorescent probe in our LCE shows the positive dichroism^{32,33} (**Figure S3**), the bright part indicates the richer component of \mathbf{n} projected to the polarizer axis set in the x axis here. The tangibly longer shape of the bright rectangular domains in $+45^\circ$ or -45° orientation to the x axis appears. This orientational correlation is also clearly seen in their autocorrelation function images (ACF), $ACF(\mathbf{r}) = \langle n_x(\mathbf{r})n_x(\mathbf{r}_0 - \mathbf{r}) \rangle_{\mathbf{r}_0}$, where $n_x(\mathbf{r})$ is the PFOM intensity at the image position \mathbf{r} , and of their fast Fourier transformed (FFT) ones (**Figure 1d, bottom**). Since this character remains even on sample rotation (**Figure S4, Movie S1**), the overall director configuration is macroscopically isotropic, being consistent with the WAXS pattern of the polydomain texture. Thus, $ACF(\mathbf{r})$ approximately corresponds to the *relative* orientational correlation function,^{35,40} $G_{\text{rel}}(\mathbf{r})$, of \mathbf{n} in the polydomain structure. Here, $G_{\text{rel}}(\mathbf{r}) = \langle ACF(\mathbf{r}) \rangle_{\text{sample-rotation}}$, with the average over rotational angle of the sample while keeping polarizers aligned in the x direction. The four-leaves pattern of the FFT image qualitatively corresponds to the DPLS pattern obtained under a conoscopy setup (**Figure S5**), supporting that PFOM captures the characteristic director orientations identical to that obtained via the transmitted polarized light.

Uchida³⁵ has first theoretically predicted that the similar pattern with the $\pm 45^\circ$ director correlation³⁶ appears as a consequence of the elastic interaction between the neighboring domains, coupled to their nematic order. This is simply because additional strain due to

spontaneous elongations upon emergence of the nematic order in domains are locally accommodated in adjacent domains without macroscopic deformation. Our 3D observation using confocal PFOM with the higher spatial resolution (**Figure 1f, Movie S2**) confirms that the pattern ubiquitously spans over the bulk of the samples. Note that also in the z - x cross section, the longer $\pm 45^\circ$ director correlation shown by the white dashed lines is found and, in contrast, in the z - y cross section such a correlation pattern is rarely found. This is reasonable as the z - x plane is symmetrically identical to x - y one upon observation with polarizers in the x direction.

Further analysis of ACF reveals the anisotropic feature of polydomain texture (**Figure 5c-e**). The radially averaged ACF, $ACF_{\text{rad-av}}$, gives a typical measure of the spatial director correlation $G(r) = \langle \mathbf{n}(r) \cdot \mathbf{n}(0) \rangle$, as $G(r) \sim \langle G_{\text{rel}}(\mathbf{r}) \rangle_{\text{rad-av}}$, with the radial averaging over separation r . The characteristic domain lengths, ξ_D , extracted as the first minimum of $ACF_{\text{rad-av}}$, for both LCE materials show a similar value of order $1 \mu\text{m}$, which is commonly observed for various LCE.¹ Another characteristic length, ξ_{av} , corresponding to the average periodicity of domains, appears as $\sim 2.2 \mu\text{m}$, which represents the average distance over which \mathbf{n} rotates by an angle π . The other anisotropic characteristic lengths, ξ_{diag} , ξ_{short} and ξ_{long} are also extracted from ACFs, which are defined in **Figure 5d** and may be useful for detailed characterization of the phase transition. Note that the effective crosslink density has little effect on these lengths (**Figure 5e**).

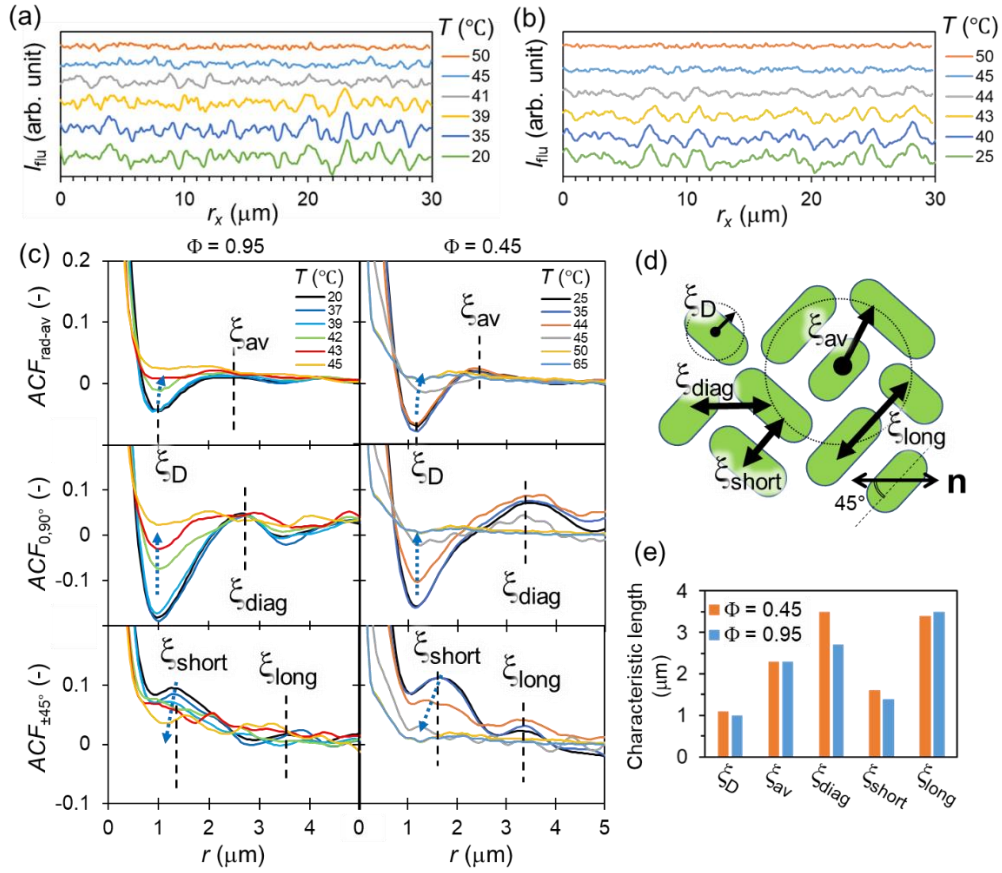


Figure 5. Characteristic lengths upon phase transition. (a) T -dependent PFOM intensity profiles (a) along the line between yellow triangles in **Figure 1d** ($\Phi = 0.95$) and (b) ($\Phi = 0.45$). (c) Characteristic lengths of polydomain structures at different T . (left column) $\Phi = 0.95$ and (right column) $\Phi = 0.45$. (top row) ACF_{rad-av} is radially averaged spatial ACF, which are normalized to hold $|ACF_{rad-av}| \leq 1$. (middle row) $ACF_{0,90^{\circ}}$ and (bottom row) $ACF_{\pm 45^{\circ}}$, where subscript numbers are angles from the polarizer direction. Several characteristic lengths are shown, where ξ_D and ξ_{av} are lengths with the minimum and the first maximum in ACF_{rad-av} , respectively, ξ_{diag} is that with the first maximum of $ACF_{0,90^{\circ}}$, and ξ_{short} and ξ_{long} are those with the first and second maxima of $ACF_{\pm 45^{\circ}}$, respectively. (d) Schematic polydomain structure on PFOM. The characteristic lengths, ξ_D , ξ_{av} , ξ_{diag} , ξ_{short} and ξ_{long} , are shown. (e) Characteristic lengths extracted from ACF, which are almost constant upon phase transition.

The POM image (**Figures 1e and S4e-h**) showing a spotted pattern^{37,41,42} is qualitatively different from PFOM as expected from their different observation principles. Although the length scale of the periodicity is similar to PFOM one, the understanding regarding \mathbf{n} is not easy because the de-polarized transmitted light at the bright parts has passed through multiple randomly-oriented birefringent domains in the present sample thickness of $\sim 5 \mu\text{m}$. Nevertheless, the observed spotted POM patterns with a certain contrast are good indicators for existence of birefringent nematic domains at the micron scale and their average intensity can be related to Q as described in **Methods** and discussed later.

***T*-dependent polydomain textures.** *T*-dependent PFOM and POM images are also shown in **Figure 3**. Unexpectedly, PFOM images and the profiles (**Figure 5a,b**) show that the initial polydomain patterns simply fade with *T*, with little change in their pattern. The almost identical patterns with simply decreased amplitudes are found over their $T_{\text{NI}} \sim 40$ and 43°C for samples with $\Phi = 0.95$ and 0.45 , respectively. ACF of PFOM images (**Figure 5c-e**) clearly support this picture, showing that the main peak and valley positions stay almost unchanged across the whole range of temperatures during the transition.

The qualitatively identical behaviour is also found in POM images with a monochromatic light. Due to the lower signal-to-noise ratio, it is difficult to evaluate accurately how the polydomain patterns survive over T_{NI} both on PFOM and conventional POM images. In contrast, the POM images with slightly de-crossed polarizers (**Figure 3a-b, bottom rows**), which also show quasi-periodic patterns with the similar periodicity of order $1 \mu\text{m}$, is more sensitive to the spatial difference in birefringence, and thus, is useful for further evaluation. Surprisingly, the de-crossed POM images with the quasi-periodic patterns suggest that the

similar polydomain structures retain at least over $\Delta T \sim 17$ and $\sim 5^\circ\text{C}$ above their T_{NI} for LCE prepared with $\Phi = 0.95$ and 0.45 , respectively, without any indication of divergence in characteristic lengths. It also indicates that the local elastic constraints preserve the (para)nematic order well above the nominal transition point. Since these ΔT suggest the lower bounds limited by the microscopy resolution, polydomain structures may remain for even larger temperature range. T -dependent DPLS patterns of different thicknesses (Figures 6, 7, S6, S7), which correspond to POM images in the reciprocal space, also show no noticeable change in scattering curve shapes. They simply fade with T . Overall these results support the concept of a diffuse N-I transition in polydomain LCE.

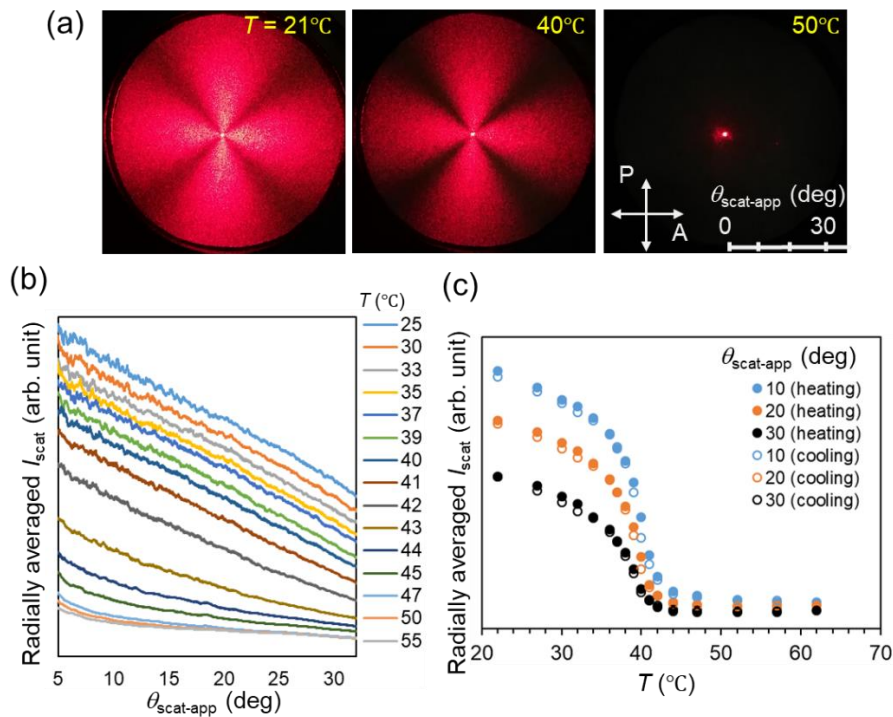


Figure 6. N-I transition characterised by depolarized light scattering (DPLS) method on LCE ($\Phi = 0.95$). (a) Typical DPLS patterns at different T . The Maltese cross suggests that the nematic domains with the director in the $\pm 45^\circ$ directions from the polarizers have longer correlation in the two orthogonal directions of polarizers. This result corresponds well to FFTs of the PFOM images. In the pattern at $T = 50^\circ\text{C}$, the peak at the centre and the scattering at small angle would be caused by the stray light associated with the present experimental setup. (b) The radially averaged scattering intensity, I_{scat} , at different T upon heating. Note that there is no peak. (c) Plots of I_{scat} vs. T at different apparent scattering angles, $\theta_{\text{scat-app}} = 10, 20,$ and 30° , which correspond to length scales of \sim of $\sim 3.6, \sim 1.8$ and $\sim 1.3 \mu\text{m}$, respectively. The data on both heating and cooling, which show few hysteresis, are shown.

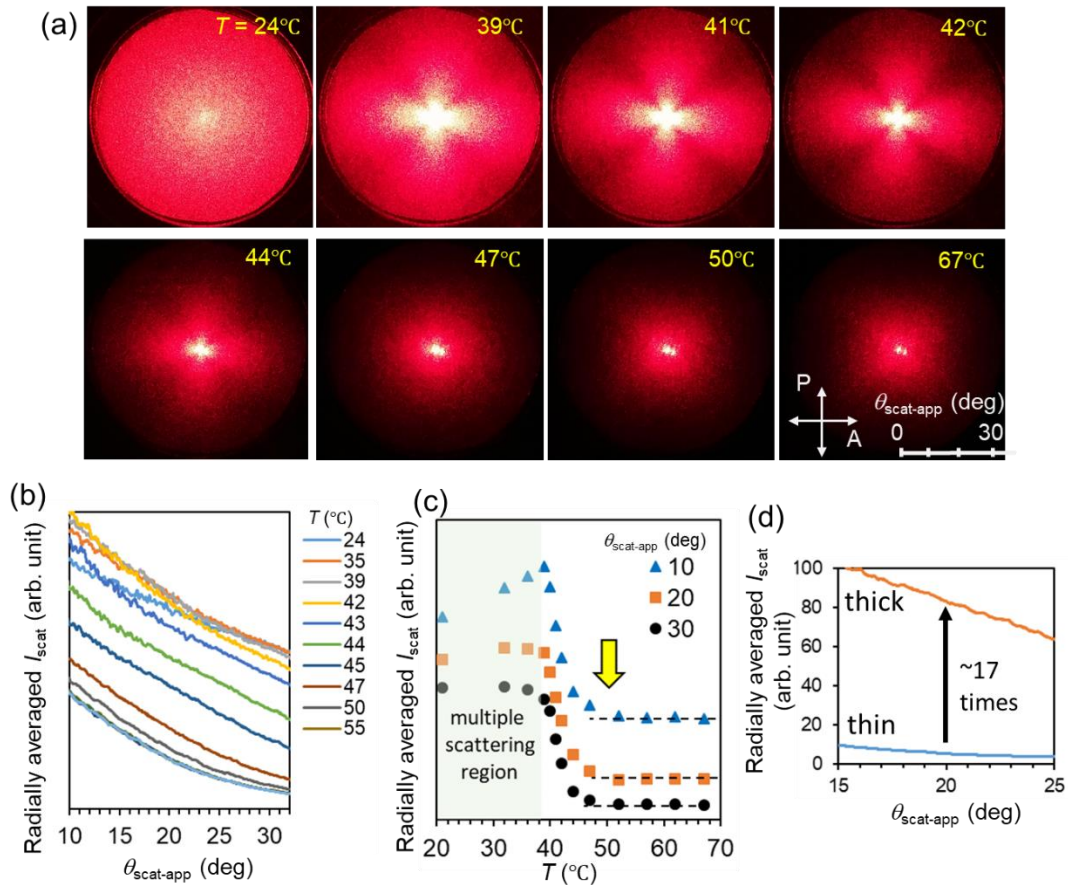


Figure 7. N-I transition characterised by DPLS method on thicker LCE ($\sim 90 \mu\text{m}$) ($\Phi = 0.95$). (a) Typical DPLS patterns at different T . The Maltese cross become visible above $\sim 40^\circ\text{C}$ due to the decrease of the total strong multiple scattering, i.e., clearing. It is noted that the cross is still visible at $\sim 47^\circ\text{C}$. (b) The radially averaged scattering intensity, I_{scat} , at different T upon heating. Note that there is no peak. (c) Plots of I_{scat} vs. T at different apparent scattering angles, $\theta_{\text{scat-app}} = 10, 20,$ and 30° , which correspond to length scales of $\sim 3.6, \sim 1.8$ and $\sim 1.3 \mu\text{m}$, respectively. The data below $\sim 43^\circ\text{C}$ are different from the thin sample case (Figure 6). The lower T range is difficult to be discussed and should be discarded. (d) The comparison of the radially averaged I_{scat} of thin and thick samples at $T = 45^\circ\text{C}$. The scattering intensity of thick sample is ~ 17 times larger than the thin one, which roughly corresponds to the thickness ratio; $(90 \mu\text{m})/(\sim 5 \mu\text{m})$. This strongly indicates that the birefringent pattern observed by POM is not attributed to the effects from surface or interface, i.e., boundary effect, and it exists throughout the bulk.

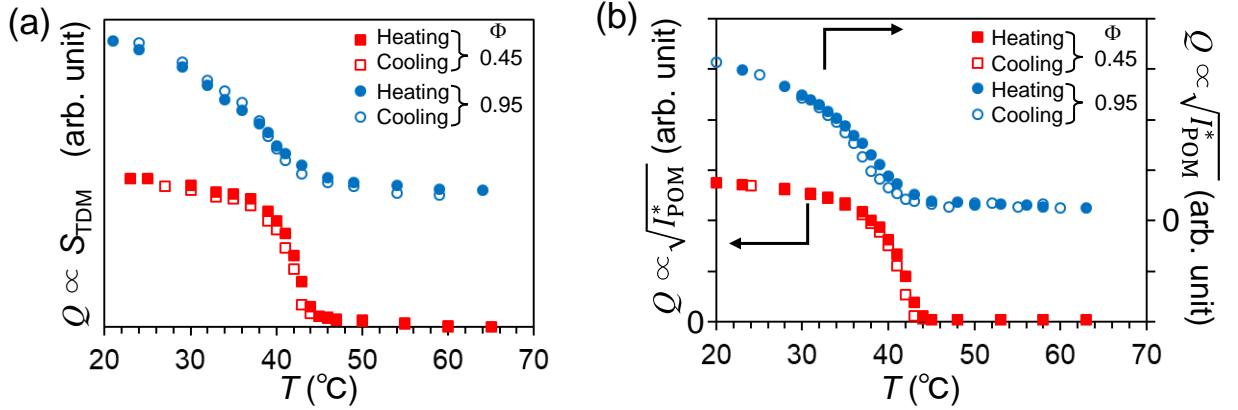


Figure 8. Order parameter upon phase transition. (a) T -dependent local order parameter of the transition dipole moment of the fluorescent probe, S_{TDM} , which corresponds to the local nematic scalar order parameter Q . (b) Square root of T -dependent transmittance of POM images, $\sqrt{I_{\text{POM}}^*}$, which is also related to Q through the birefringent $\Delta n(T)$. Both S_{TDM} and $\sqrt{I_{\text{POM}}^*}$ suggest the diffuse transition with little hysteresis.

Order parameter Q upon phase transition. **Figure 8** shows a set of $Q(T)$ -related values associated with our LCE, S_{TDM} and $\sqrt{I_{\text{POM}}^*}$, which are separately derived using PFOM and POM, respectively (see **Methods** with **Figure S8** for details). These curves also suggest the transition without thermal hysteresis. Broadening of the transition appears more clearly on LCE prepared with $\Phi = 0.95$. Curves of S_{TDM} and $\sqrt{I_{\text{POM}}^*}$ agree well despite the difference in the method principle, which is based on fluorescent dichroism or birefringence, confirming their common origin, Q . Additionally, the similar diffuse transition also appear in curves for the T -induced recovery of the original length from their elongated state^{1,30,43} (**Figure S9**), supporting the validity of the presently proposed two methods for evaluation of Q .

One may wonder that the diffuse transition nature may originate from the boundary effects on the present thin sample with the thickness of $\sim 5 \mu\text{m}$. To check this the thicker samples with the thickness of $70\sim 90 \mu\text{m}$ are also evaluated using POM (**Figure S10**) and DPLS (**Figure 7 and S7**). Although the higher scattering in the thicker sample sacrifices the evaluation at lower T , the diffuse transition like those obtained for thin samples is reproduced safely at $T > T_{\text{NI}}$. The results eliminate the boundary effect on the diffuse transition, i.e., it is the bulk nature of the present LCE.

According to the related theory based on the phenomenological Landau-de-Gennes model with quenched random disorder,^{22,24} the higher disorder boosts the supercriticality of the N-I transition. Thus, the observed difference in the transition found in LCE with different degrees of quenched disorder associated with the effective crosslink density is qualitatively amenable to the theory. Certain disorders have been imprinted in the polymer network

including inhomogeneities of chemical crosslinks, entanglements, polydispersity of strand lengths, and heterogeneities of components. They generally suppress the reconfiguration and relaxation of network strands toward the ideal isotropic state and would leave slight nematic order above the transition especially on the main-chain LCE with less rotational flexibility of mesogens. Thus, such disorders may stabilize the paranematic state, diffusing the transition.

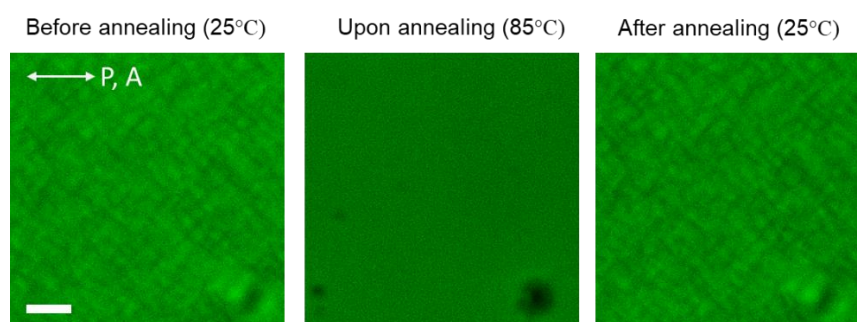


Figure 9. Memory of the polydomain structure after annealing beyond polymerization temperature. On the LCE sample with $\Phi = 0.95$ the polydomain structure before and after thermal annealing at 85°C for 3 hours were compared at a certain location (with the peculiar point at the bottom-right for the guide to find the location) using PFOM. The images roughly coincide with each other, suggesting that the network heterogeneity imprinted on the polymer network is stable against the present level of thermal fluctuation. (Bar: $5\ \mu\text{m}$)

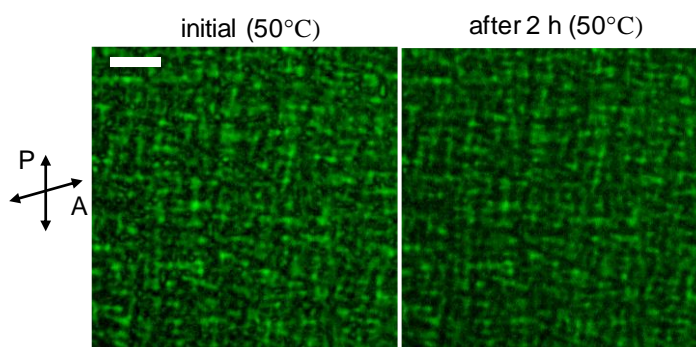


Figure 10. Stable polydomain structure at 10 K higher than T_{NI} . On the LCE sample with $\Phi = 0.95$ the polydomain structure observed at 50°C , which is 10 K higher than T_{NI} , for one hour by POM with slightly de-crossed polarizers to trace the polydomain structure with small birefringence. The spotted pattern unchanged at least for two hours. (Bar: $5\ \mu\text{m}$)

Discussion

Focusing on the polydomain size, it is surprising that the characteristic domain lengths and anisotropic shapes are almost independent of T , and thus, of Q , i.e., $\xi_D \sim \text{const.}$, even around the transition point (**Figures 3 and 5**). The result differs from previous experiments based on the DPLS on a side-chain LCE³⁷ and a non-crosslinked LC polymer,⁴¹ which suggested the divergence of ξ_D , and from proposed models for crosslinked LCE,^{34,35} which basically assume the competition between Q and the quenched random disorder to give rise to ξ_D , and thus, ξ_D scales with Q . The present results may be explained by considering the existence of a strong reference state that induces a specific polydomain structure insensitively to Q and firmly survives above T_{NI} . The reference state may have formed upon the polymerisation as the inherent heterogeneity in ordinary polymers.⁴⁴⁻⁴⁹

It is important to confirm whether the observed polydomain is unique one, which is independent of the thermal history, or not. After thermal annealing at isotropic temperature followed by cooling, LCE prepared with $\Phi = 0.95$ recovers initially observed polydomain patterns almost perfectly at the same location (**Figure 9**). Moreover, it is also insensitive to the cooling rate within the accessible time scale. Additionally, the LCE was observed with the slightly de-crossed POM at 50°C , which is 10 K higher than T_{NI} , for hours, showing no

noticeable change, e.g., coarsening,^{41,50} on the spotted pattern corresponding to the polydomain texture (**Figure 10**). These results indicate that the polydomain state with specific ξ_D on the present main-chain LCE is insensitive to T and the annealing time. Thus, ξ_D would be uniquely identified by an inherent heterogeneity imprinted upon polymerisation. This is different from the idea suggested by Duzgan et al,³⁶ in which ξ_D is kinetically determined.

At present we cannot assign the origin of the relevant heterogeneity, which may exist as various disorders in the polymer network with multiple correlation length scales. The quenched random disorder introduced by crosslinkers^{21,24} has been assumed to be the main origin of equilibrium polydomain texture and the diffuse transition in LCE. However, the additional heterogeneity on a larger scale must also be relevant in the polydomain structure, where the local elastic strains in each elongating domain must find a complex compatibility pattern, thus creating a strong local elastic field coupling to the order parameter in de Gennes' manner. Such strong internal constraints cause the domain size ξ_D to be insensitive to T , Q , and the effective Frank elastic constants, since the energy scale of local elastic interactions is several orders of magnitude greater than the Frank or Landau-de Gennes energies. This is contrast to the effect of quenched random disorder on ξ_D previously discussed theoretically,^{34,35} where the physics was based on the competition of disorder and the Frank elasticity. Detailed analysis on the polymer network heterogeneity^{44-46,49} using, e.g., the neutron scattering, and on its growth during complex polymerization, e.g., microsineresis^{47,48} effects, would help further discussion on the origin of ξ_D and remain to be studied. Finally, the comparison to the previous case of a side-chain LCE,³⁷ which exhibits

T -dependent ξ_D , also suggests that the presently observed constant ξ_D may be related uniquely to the lower flexibility of the mesogenic units incorporated into the main-chain polymer network³⁰ with crosslinks.

Conclusions

In summary, we experimentally show that our main-chain LCE exhibit a diffuse N-I transition of supercritical nature, approaching the critical point when the material is prepared with less chain entanglement. New methods to estimate the nematic order Q on the polydomain LCE from fluorescence dichroism and birefringence obtained by the polarized microscopies are developed. The polarized and fluorescence optical microscopies also reveal that the characteristic polydomain structure with anisotropic relative director correlation surviving at least 5~17 K above T_{NI} , depending on the effective crosslink density. Little sensitivity of the domain size to $Q(T)$ raises questions on the origin of the polydomain pattern on main-chain LCE. Practically, present simple and versatile methods to characterize the nematic transition of LCE will be useful for their optimization toward dynamic applications that rely on the phase transition nature.

Methods

Materials and preparation of LCE. For preparation of LCE, we slightly modified the methods reported previously,^{7,27-29} in which single-step crosslinking reaction of a thiol-acrylate Michael addition is used. The diacrylate monomer, 1,4-bis-[4-(6-acryloyloxyhexyloxy)benzoyloxy]-2-methylbenzene (RM82), was purchased from Wilshire Technologies ([Scheme S1](#)). The diacrylate spacer, tri(propylene glycol) diacrylate (TPGDA,

isomer mixture), and two thiol monomers: 2,2'-(ethylenedioxy) diethanethiol (EDDET) and pentaerythritol tetrakis (3-mercaptopropionate) (PETMP), were purchased from Sigma Aldrich. Triethylamine (TEA, Sigma Aldrich) was used as the catalyst of the Michael-addition thiol-ene reaction. As the radical scavenger, butylated hydroxytoluene (BHT, from Sigma Aldrich) was used to suppress the unwanted reaction between acrylates. As the dichroic fluorescent probe, coumarin 545T (C5T, Tokyo Chemical Industry)⁵¹ was used. Dimethylformamide (DMF, Sigma Aldrich) and toluene (Sigma Aldrich) were used as the solvents. All chemicals were used in their as-received condition with no purification.

At the specific molar ratio of functional groups shown in [Scheme S1](#), RM82, TPGDA, EDDET and PETMP were weighed, BHT was added at 0.5wt%, DMF solution of C5T was added to make the final dye concentration after solvent evaporation to be 0.01wt%, and toluene was added at 0 or 50wt%. Note that the amount of the solvent was important to control the effective crosslink density via effective degrees of polymerization and of network entanglements, which would also work as the cross-linking point. The former (0%) or latter (50%) case, the mass fraction Φ of the polymer content in relation to solvent on the reaction was ~ 0.95 or 0.45 , respectively. The more amount of solvent, the less entanglement⁵² and slightly lower polymerization degree are expected. After the mixture was gently mixed at an elevated $T \sim 70^\circ\text{C}$ for ~ 10 min, TEA was added at 1.5~3wt% to start the Michael-addition reaction between thiol and acrylate groups. The mixture was kept between two glass slides with the spacer with ~ 0.09 mm at 75°C (isotropic phase) overnight. For thin sample, a wedge cell was used with the spacer of 15~30 μm . For the thin sample, which was mainly evaluated in this study, one side of the glass mold was removed and placed in an oven at 75°C overnight for de-swelling. The thick sample was released from the glass mold, and

placed in the oven at 75°C overnight for de-swelling. For the thick samples with toluene, which showed larger volumetric shrinkage, samples were de-swelled on the water to minimise the external constraint. For the thin samples with toluene, the constraint of the substrate would cause the uniaxial compression in the thickness direction. This would make the macroscopic alignment be slightly anisotropic with the negative order parameter with respect to the sample normal while keeping the in-plane homogeneous orientational distribution. Although the resultant effect on the phase transitions appeared negligible, note the possible difference in the internal stress state according to the thickness of the present sample with toluene upon polymerisation. Every sample was then placed in a vacuum oven at 75°C at least ~12 hrs to ensure the solvent evaporation prior the characterization.

Optical microscopy. We observed LC alignment using a transmitted polarizing optical microscope (POM) (BX-51P, Olympus) under crossed-nicols conditions. The light source was white or monochromatic (530 nm) light, depending on the experiments. When, in general, the LCE sample has birefringence locally within each domain with the length scale comparable to the optical resolution, a certain amount of light can be depolarized depending on the position showing a certain pattern, which *indirectly* reflects the nematic domain structure. For example, the bright parts suggest that the local effective birefringence (optical anisotropy), i.e., the refractive index difference Δn_{eff} , on the transmittance is large through the thickness, which is here ~5 μm . Since it is not expected that the director is homogeneous through this thickness, it is not possible to extract the domain structure, such as the domain length or correlation length, from this POM image. Nevertheless, the existence of a certain

pattern on the POM image clearly indicate that the sample has birefringent domains with the scale of the optical resolution of several hundreds of nanometres.

To observe fluorescent images, we used a conventional fluorescence optical microscope (FOM), where the light source was mounted above the sample and the excitation light passed through the microscope objective lens on its way toward the sample. A Xe lamp (75W) was used as the light source. To detect the emission from fluorescence probes, we used a fluorescence filter set (U-MWIB-3, Olympus) comprising an excitation filter that transmitted light with wavelengths between 460 nm and 495 nm, and an emission filter that transmitted light with wavelength larger than 510nm. The images were collected at the pixel size of 0.154 μm using a Nikon DS-Ri2 camera connected to a computer and controlled through imaging software (NIS-Elements, Nikon). An objective lens with a numerical aperture (NA) of 0.75 (MPLFLN-BDP50x, Olympus) was mainly used.

To observe the polydomain the linearly polarized excitation was used and the polarized fluorescence intensity in the identical polarization was measured (PFOM). The focus was carefully adjusted to the top surface, where the contrast became highest. With the positive dichroic dye, which is used here, the dichroic contrast is enhanced.³³ On PFOM images, the brighter parts indicate that the absorption and fluorescence transition dipole moment (TDM) vectors of the probe have more components in the polarizer direction. Since the present dye molecules align parallelly to the nematic directors of the LCE (**Figure S3**), domains resolved by PFOM directly reflect the polydomain structure in two-dimension (2D). Given the polarizers along the x axis, the fluorescence intensity reflects the x component, n_x , of the director \mathbf{n} . If the polarizers (or the sample) is rotated, the brightest or darkest part gradually becomes darker or brighter, respectively (**Figure S4, Movie S1**).

Temperature, T , at the sample was controlled on a transparent hot-stage (Tokai-Hit) with the multiple thermocouples around the observation point. T was changed at the rate less than $\sim 0.01^\circ\text{C/s}$.

Two methods for local nematic order estimation. The local order parameter Q of the LCE was estimated through two essentially different methods using POM and PFOM images as described below. The former and latter are based on the birefringence of the sample and on the dichroic property of the fluorescent dye aligning with \mathbf{n} , respectively.

POM image-based nematic order estimation. The POM image taken with monochromatic light $\lambda = 530$ nm was used for this analysis. In the present LCE, we can safely assume that axes of birefringent sources, i.e., \mathbf{n} , are *macroscopically* homogeneous in the sample plane (**Figures S1 and S4**). Here, we note the relationship between the total transmittance of the POM image under the crossed-nicols condition, I_{POM}^* , and the local refractive index difference Δn , which is approximately related to the local scalar order parameter^{1,53} as $\Delta n \propto Q$. We consider a birefringent volume element at the position (x, y) with the effective birefringence $\Delta n_{\text{eff}}(x, y)$ and with the thickness, t , in which $\theta^*(x, y)$ is the effective orientation of \mathbf{n} projected onto the xy -plane and $\delta(x, y)$ is the effective optical path difference, $\delta(x, y) \sim \frac{2\pi}{\lambda} \Delta n_{\text{eff}}(x, y) t$. Due to the macroscopically homogeneous distribution of \mathbf{n} , we may assume that $\Delta n_{\text{eff}}(x, y)$ is independent of position, and thus, $\Delta n_{\text{eff}} \propto \Delta n$. Then, the total transmittance under the crossed nicol condition leads $I_{\text{POM}}^* \sim \int_{\text{area}} \sin^2 2\theta^* \sin^2 \frac{\delta}{2} \propto \sin^2 \frac{\delta}{2}$, considering the homogeneous distribution of $\theta^*(x, y)$ on the image of interest. Finally, $Q \propto \Delta n \propto \sin^{-1} \sqrt{I_{\text{POM}}^*}$, and for small $\sqrt{I_{\text{POM}}^*}$, $Q \propto \sqrt{I_{\text{POM}}^*}$. Since it is experimentally impossible

to obtain the real zero intensity because of the stray light, the final relationship should be written as $Q \propto \sqrt{I_{\text{POM}}^*} - C$, where C is the unknown offset. Nevertheless, the phase transition nature can be captured from T -dependent curve of $\sqrt{I_{\text{POM}}^*}$. Note that this analysis is only possible with the low scattering sample or state, which is here achieved by using the thin sample. If the thick sample ($\sim 80 \mu\text{m}$) was used, non-negligible amount of the incident light is scattered out of the NA due to the multiple scattering at lower T , with expectedly the higher Δn . Even with the thick sample, there is a chance to correct the reliable transmittance due to the decrease in Δn at higher T (**Figure S10**), which is more reliable due to the higher signal-to-noise ratio when we focus on the diffuse transition nature with small but non-zero Q , and thus, Δn slightly above T_{NI} .

PFOM image-based nematic order estimation. Here, from the local fluorescence dichroic ratio R , we obtain the order parameter of TDM on the fluorescent probe, S_{TDM} , which should be closely related to the local nematic scalar order parameter Q along the director $\mathbf{n} = (n_x, n_y, n_z) = (\cos \theta \cos \phi, \sin \theta \cos \phi, \sin \phi)$. On the present PFOM images, the polydomain structure is reflected as the contrast of the fluorescence intensity $I_{\text{flu}}(x, y)$. If one focus on a certain position and rotate sample (or polarizers), $I_{\text{flu}}(x, y)$ should oscillate as $I_{\text{flu}}(x, y) \sim [I_{\text{max}}(x, y) - I_{\text{min}}(x, y)] \cos^2[\Omega - \theta(x, y)] + I_{\text{min}}(x, y)$, where Ω is the angle of polarizers and I_{max} and I_{min} are the maximum and minimum intensity at the position (x, y) , respectively. The amplitude of the oscillation is further related to the polar angle, ϕ , of \mathbf{n} as $[I_{\text{max}}(x, y) - I_{\text{min}}(x, y)] \sim \Delta I_{\text{max}} \cos^2 \phi(x, y)$. The local dichroic ratio R corresponds to $(I_{\text{max}}/I_{\text{min}})^{1/2}$ at $\phi = 0$, where the power of $1/2$ is due to the polarized excitation setup.³³ Ideally, by rotating polarizers and finding the global maximum and minimum intensity, R

can be determined. Considering the background noise and the statistical reliability, we may alternatively use the standard deviation σ of the distribution of $I_{\text{flu}}(x,y)$ to estimate R . Since the macroscopic orientational distribution of \mathbf{n} is homogeneous, $I_{\text{flu}}(x,y)$ should distribute around an averaged value I_{ave} and theoretically equals to $\frac{I_{\text{max}}-I_{\text{min}}}{2}$. As a first approximation, we may define as $I_{\text{max}} = I_{\text{ave}} + 2\sigma$ and $I_{\text{min}} = I_{\text{ave}} - 2\sigma$, which correspond well to the maximum and minimum on the line profiles (**Figure S8**). Using the obtained $R = (I_{\text{max}}/I_{\text{min}})^{1/2}$, S_{TDM} can be calculated as $S_{\text{TDM}} = \frac{R-1}{R+2}$. It is noted that the absolute value of S_{TDM} is problematic because PFOM signals also contain background noise and have inherently no z -resolution, and thus, are disturbed by the fluorescence from the out-of-focus plane, in which other domains with different \mathbf{n} exists. Nevertheless, the effects only add the baseline shift and simple multiplication of the real S_{TDM} , and thus, the phase transition nature can be captured from the T -dependent curve shape of S_{TDM} .

Note that both values, S_{TDM} and $\sqrt{I_{\text{POM}}^*}$, cannot be the measure of the local order parameter smaller than the optical resolution, which is approximately in the order of the wavelength of the observation light, $\sim 0.5 \mu\text{m}$, in contrast to NMR methods^{25,26} with fine resolution. Nevertheless, the present methods are simple and versatile as they only require thin sample and doping of fluorescent probes for the PFOM case.

3D PFOM by confocal laser scanning microscopy. A confocal laser scanning FOM (A1⁺ system, Nikon) was used to obtain PFOM images at 25°C (nematic). An optically pumped semiconductor laser (LU-N4 Laser Unit, Nikon, equipped with Sapphire 488, Coherent Inc.) was used to excite the fluorescent molecules at 488 nm and the emitted light between 525 and 595 nm was collected. An objective lens with an NA of 1.45 (PlanApoTIRF100 \times , oil,

Nikon) was used for the sample with a cover glass. Images were acquired at the voxel size of typically $30(x) \times 30(y) \times 50(z)$ nm³. The excitation laser was linearly polarized and emitted fluorescence in the same polarization was collected using a polarizer.

Depolarized light scattering (DPLS). For DPLS measurement,³⁷ a He-Ne laser (wavelength of 632.8 nm, 1 mW, Melles Griot 05-LHP-111) was used. The sample was placed between a set of polarizers under crossed-nicol condition, which is often called as the HV mode. The laser light diameter was ~0.6 mm. The scattering pattern on a paper screen placed at the distance of 30 mm from the sample was captured by a digital camera. The same position on the sample, at which the microscopy was performed, was observed under the *T*-controlled setup.

Dynamic scanning calorimetry (DSC). For differential scanning calorimetry (DSC6100 SII Nanotechnology), samples with approximately 15 mg were loaded into standard aluminium DSC pans. The samples were heated to 90°C at 10°C/min, held isothermally for 5 min, and cooled to -60°C at 5°C/min to acquire the data. The nematic-isotropic transition peak can be found at local minimum of the endothermic peak. The sample was run three times.

Stress-strain response. The stress-strain curves for LCE films on the tensile mode were obtained using a commercial instrument (EMX1000, IMADA). The sample width, thickness and effective length were, 5 mm, 0.8 mm and 30 mm, respectively. Strain was increased until the sample break at the extension rate of 0.00042 s⁻¹.

Wide angle X-ray scattering (WAXS). The phase of the present LCE at RT was characterized using a Philips diffractometer using a Philips Copper target (PW-2233/20) with the wavelength of 0.154 nm. The distance between the sample and the imaging area was 100 mm.

ASSOCIATED CONTENT

Supporting Information. Supplementary information accompanies this paper at XXX.

Materials, WAXS pattern, Fluorescence spectrum, PFOM images under uniaxial strain, PFOM and POM images with different polarizers configurations, POM at conoscopy setup, DPLS patterns at various temperatures, profile analysis of PFOM intensity, temperature-dependent strain, and comparison of POM intensity between different sample thicknesses (PDF), PFOM and confocal PFOM images on movies (AVI)

AUTHOR INFORMATION

Corresponding Author.

Takuya Ohzono, Research Institute for Electronics and Photonics, National Institute of Advanced Industrial Science and Technology (AIST), 1-1-1 Higashi, Tsukuba 305-8565, Japan, E-mail: ohzono-takuya@aist.go.jp ORCID: <https://orcid.org/0000-0003-2185-2504>

Author Contributions. T.O. conceived the central idea. T.O. performed the main experiments. K.K. and T.O. performed observations using confocal-PFOM. The results were analyzed by T.O. and E.M.T., T.O and E.M.T wrote the manuscript, and all authors discussed the results and the manuscript.

Funding Sources. This work was supported by the European Research Council grant No: 786659 (E.M.T.) and partly by JSPS KAKENHI Grant Number JP 20K20967 (T.O.) and MEXT KAKENHI Grant Numbers JP 17H06417 and JP 17H06413 (K.K.).

ACKNOWLEDGMENT This work was supported by the European Research Council grant No: 786659 (E.M.T.) and partly by JSPS KAKENHI Grant Number JP 20K20967 (T.O.) and MEXT KAKENHI Grant Numbers JP 17H06417 and JP 17H06413 (K.K.). The authors are grateful for many useful communications from Y. Norikane, E. Koyama, K. Saitoh, Y. Kikkawa, M. Yoneya, T. Mizokuro, Y. Sonoda, K. Urayama, C. Zannoni, M. O. Saed, and H. Minamikawa.

REFERENCES

- (1) Warner, M., Terentjev, E. M. *Liquid Crystal Elastomers*; Oxford Univ. Press, 2007.
- (2) Hébert, M.; Kant, R.; De Gennes, P. G. Dynamics and Thermodynamics of Artificial Muscles Based on Nematic Gels. *J. Phys. II* **1997**, *7* (7), 909–919. <https://doi.org/10.1051/jp1:1997209>.
- (3) Yu, Y.; Nakano, M.; Ikeda, T. Directed Bending of a Polymer Film by Light. *Nature* **2003**, *425* (6954), 145–145. <https://doi.org/10.1038/425145a>.
- (4) Ohm, C.; Brehmer, M.; Zentel, R. Liquid Crystalline Elastomers as Actuators and Sensors. *Adv. Mater.* **2010**, *22* (31), 3366–3387. <https://doi.org/10.1002/adma.200904059>.
- (5) White, T. J.; Broer, D. J. Programmable and Adaptive Mechanics with Liquid Crystal Polymer Networks and Elastomers. *Nat. Mater.* Nature Publishing Group 2015, pp 1087–1098. <https://doi.org/10.1038/nmat4433>.
- (6) Liu, D.; Broer, D. J. Self-Assembled Dynamic 3D Fingerprints in Liquid-Crystal Coatings towards Controllable Friction and Adhesion. *Angew. Chemie - Int. Ed.* **2014**, *126* (18), 4630–4634.
- (7) Ohzono, T.; Saed, M. O. M. O.; Terentjev, E. M. E. M. Enhanced Dynamic Adhesion in Nematic Liquid Crystal Elastomers. *Adv. Mater.* **2019**, *31* (30), 1902642. <https://doi.org/10.1002/adma.201902642>.
- (8) Ohzono, T.; Norikane, Y.; Saed, M. O.; Terentjev, E. M. Light-Driven Dynamic Adhesion on Photosensitized Nematic Liquid Crystalline Elastomers. *ACS Appl. Mater. Interfaces* **2020**, *12* (28), 31992–31997. <https://doi.org/10.1021/acsami.0c08289>.
- (9) Liu, D.; Broer, D. J. Light Controlled Friction at a Liquid Crystal Polymer Coating with Switchable Patterning. *Soft Matter* **2014**, *10*, 7952–7958. <https://doi.org/10.1039/c4sm01249f>.
- (10) Ohzono, T.; Saed, M. O.; Yue, Y.; Norikane, Y.; Terentjev, E. M. Dynamic Manipulation of Friction in Smart Textile Composites of Liquid-Crystal Elastomers. *Adv. Mater. Interfaces* **2020**, *1901996*, 1–7. <https://doi.org/10.1002/admi.201901996>.
- (11) Brannum, M. T.; Steele, A. M.; Venetos, M. C.; Korley, L. S. T. J.; Wnek, G. E.; White, T. J. Light Control with Liquid Crystalline Elastomers. *Adv. Opt. Mater.* **2019**, *7* (6), 1–7. <https://doi.org/10.1002/adom.201801683>.
- (12) de Gennes, P. G.; Prost, J. *The Physics of Liquid Crystals*, 2nd ed.; Oxford Univ. Press: New York, 1993.
- (13) Schätzle, J.; Kaufhold, W.; Finkelmann, H. Nematic Elastomers: The Influence of External Mechanical Stress on the Liquid-crystalline Phase Behavior. *Makromol. Chem.* **1989**, *190*, 3269–3284. <https://doi.org/10.1002/macp.1991.021920522>.
- (14) Disch, S.; Claudia, S.; Finkelman, H. Nematic Elastomer beyond the Critical Point. *Macromol. Rapid. Commun.* **1994**, *15*, 303–310. <https://doi.org/doi.org/10.1002/marc.1994.030150402>.
- (15) Clarke, S. M.; Hotta, A.; Tajbakhsh, A. R.; Terentjev, E. M. Effect of Crosslinker Geometry on Equilibrium Thermal and Mechanical Properties of Nematic

- Elastomers. *Phys. Rev. E - Stat. Physics, Plasmas, Fluids, Relat. Interdiscip. Top.* **2001**, *64* (6), 8. <https://doi.org/10.1103/PhysRevE.64.061702>.
- (16) Thomsen, D. L.; Keller, P.; Naciri, J.; Pink, R.; Jeon, H.; Shenoy, D.; Ratna, B. R. Liquid Crystal Elastomers with Mechanical Properties of a Muscle. *Macromolecules* **2001**, *34* (17), 5868–5875. <https://doi.org/10.1021/ma001639q>.
- (17) Lebar, A.; Kutnjak, Z.; Žumer, S.; Finkelmann, H.; Sánchez-Ferrer, A.; Zalar, B. Evidence of Supercritical Behavior in Liquid Single Crystal Elastomers. *Phys. Rev. Lett.* **2005**, *94* (19), 1–4. <https://doi.org/10.1103/PhysRevLett.94.197801>.
- (18) Cordoyiannis, G.; Lebar, A.; Rožič, B.; Zalar, B.; Kutnjak, Z.; Žumer, S.; Brömmel, F.; Krause, S.; Finkelmann, H. Controlling the Critical Behavior of Paranematic to Nematic Transition in Main-Chain Liquid Single-Crystal Elastomers. *Macromolecules* **2009**, *42* (6), 2069–2073. <https://doi.org/10.1021/ma802049r>.
- (19) Selinger, J. V.; Jeon, H. G.; Ratna, B. R. Isotropic-Nematic Transition in Liquid-Crystalline Elastomers. *Phys. Rev. Lett.* **2002**, *89* (22), 2257011–2257014. <https://doi.org/10.1103/PhysRevLett.89.225701>.
- (20) de Gennes, P. G. Réflexions Sur Un Type de Polymères Nématiques. *Rend. Acad. Sci. B* **1975**, *281*, 101–103.
- (21) Fridrikh, S. V.; Terentjev, E. M. Polydomain-Monodomain Transition in Nematic Elastomers. *Phys. Rev. E - Stat. Physics, Plasmas, Fluids, Relat. Interdiscip. Top.* **1999**, *60* (2), 1847–1857. <https://doi.org/10.1103/PhysRevE.60.1847>.
- (22) Selinger, J. V.; Ratna, B. R. Isotropic-Nematic Transition in Liquid-Crystalline Elastomers: Lattice Model with Quenched Disorder. *Phys. Rev. E - Stat. Physics, Plasmas, Fluids, Relat. Interdiscip. Top.* **2004**, *70* (4), 8. <https://doi.org/10.1103/PhysRevE.70.041707>.
- (23) Pasini, P.; Skačej, G.; Zannoni, C. A Microscopic Lattice Model for Liquid Crystal Elastomers. *Chem. Phys. Lett.* **2005**, *413* (4–6), 463–467. <https://doi.org/10.1016/j.cplett.2005.08.006>.
- (24) Petridis, L.; Terentjev, E. M. Nematic-Isotropic Transition with Quenched Disorder. *Phys. Rev. E - Stat. Nonlinear, Soft Matter Phys.* **2006**, *74* (5), 1–11. <https://doi.org/10.1103/PhysRevE.74.051707>.
- (25) Feio, G.; Figueirinhas, J. L.; Tajbakhsh, A. R.; Terentjev, E. M. Critical Fluctuations and Random-Anisotropy Glass Transition in Nematic Elastomers. *Phys. Rev. B* **2008**, *78* (2), 1–4. <https://doi.org/10.1103/PhysRevB.78.020201>.
- (26) Feio, G.; Figueirinhas, J. L.; Tajbakhsh, A. R.; Terentjev, E. M. Deuterium NMR Study of Mobility and Fluctuations in Nematic and Isotropic Elastomers. *J. Chem. Phys.* **2009**, *131* (7). <https://doi.org/10.1063/1.3211107>.
- (27) Nair, D. P.; Cramer, N. B.; Gaipa, J. C.; McBride, M. K.; Matherly, E. M.; McLeod, R. R.; Shandas, R.; Bowman, C. N. Two-Stage Reactive Polymer Network Forming Systems. *Adv. Funct. Mater.* **2012**, *22* (7), 1502–1510. <https://doi.org/10.1002/adfm.201102742>.
- (28) Yakacki, C. M.; Saed, M.; Nair, D. P.; Gong, T.; Reed, S. M.; Bowman, C. N. Tailorable and Programmable Liquid-Crystalline Elastomers Using a Two-Stage Thiol-Acrylate Reaction. *RSC Adv.* **2015**, *5* (25), 18997–19001. <https://doi.org/10.1039/c5ra01039j>.

- (29) Saed, M. O.; Volpe, R. H.; Traugutt, N. A.; Visvanathan, R.; Clark, N. A.; Yakacki, C. M. High Strain Actuation Liquid Crystal Elastomers via Modulation of Mesophase Structure. *Soft Matter* **2017**, *13* (41), 7537–7547. <https://doi.org/10.1039/c7sm01380a>.
- (30) Ohzono, T.; Katoh, K.; Minamikawa, H.; Saed, M. O.; Terentjev, E. M. Internal Constraints and Arrested Relaxation in Main-Chain Nematic Elastomers. *Nat. Commun.* **2021**, *12* (1). <https://doi.org/10.1038/s41467-021-21036-3>.
- (31) Smalyukh, I. I.; Shiyanovskii, S. V.; Lavrentovich, O. D. Three-Dimensional Imaging of Orientational Order by Fluorescence Confocal Polarizing Microscopy. *Chem. Phys. Lett.* **2001**, *336* (1–2), 88–96. [https://doi.org/10.1016/S0009-2614\(00\)01471-8](https://doi.org/10.1016/S0009-2614(00)01471-8).
- (32) Ohzono, T.; Katoh, K.; Wang, C.; Fukazawa, A.; Yamaguchi, S.; Fukuda, J. I. Uncovering Different States of Topological Defects in Schlieren Textures of a Nematic Liquid Crystal. *Sci. Rep.* **2017**, *7* (1), 1–13. <https://doi.org/10.1038/s41598-017-16967-1>.
- (33) Ohzono, T.; Yatabe, T.; Wang, C.; Fukazawa, A.; Yamaguchi, S. Negative Fluorescence Anisotropy of Phosphole Oxide-Based Dyes in Nematic Liquid Crystals. *Commun. Chem.* **2018**, *1* (1), 52. <https://doi.org/10.1038/s42004-018-0055-6>.
- (34) Petridis, L.; Terentjev, E. M. Quenched Disorder and Spin-Glass Correlations in XY Nematics. *J. Phys. A: Math. Gen.* **2006**, *39* (31), 9693–9708. <https://doi.org/10.1088/0305-4470/39/31/003>.
- (35) Uchida, N. Soft and Nonsoft Structural Transitions in Disordered Nematic Networks. *Phys. Rev. E - Stat. Physics, Plasmas, Fluids, Relat. Interdiscip. Top.* **2000**, *62* (4), 5119–5136. <https://doi.org/10.1103/PhysRevE.62.5119>.
- (36) Duzgun, A.; Selinger, J. V. Dynamic Theory of Polydomain Liquid Crystal Elastomers. *Phys. Rev. Lett.* **2015**, *115* (18), 1–5. <https://doi.org/10.1103/PhysRevLett.115.187801>.
- (37) Clarke, S. M.; Terentjev, E. M.; Kundler, I.; Finkelmann, H. Texture Evolution during the Polydomain-Monodomain Transition in Nematic Elastomers. *Macromolecules* **1998**, *31* (18), 4862–4872. <https://doi.org/10.1021/ma980195j>.
- (38) Clarke, S. M.; Nishikawa, E.; Finkelmann, H.; Terentjev, E. M. Light-Scattering Study of Random Disorder in Liquid Crystalline Elastomers. *Macromol. Chem. Phys.* **1997**, *198* (11), 3485–3498. <https://doi.org/10.1002/macp.1997.021981113>.
- (39) Kutter, S.; Terentjev, E. M. Tube Model for the Elasticity of Entangled Nematic Rubbers. *Eur. Phys. J. E* **2001**, *6* (3), 221–229. <https://doi.org/10.1007/s101890170004>.
- (40) Uchida, N.; Ohzono, T. Orientational Ordering of Buckling-Induced Microwrinkles on Soft Substrates. *Soft Matter* **2010**, *6* (22). <https://doi.org/10.1039/c0sm00357c>.
- (41) Elias, F.; Clarke, S. M.; Peck, R.; Terentjev, E. M. Equilibrium Textures in Main-Chain Liquid Crystalline Polymers. *Europhys. Lett.* **1999**, *47* (4), 442–448. <https://doi.org/10.1209/epl/i1999-00407-y>.
- (42) Patil, H. P.; Liao, J.; Hedden, R. C. Smectic Ordering in Main-Chain Siloxane Polymers and Elastomers Containing p-Phenylene Terephthalate Mesogens. *Macromolecules* **2007**, *40* (17), 6206–6216. <https://doi.org/10.1021/ma0706374>.

- (43) Küpfer, J.; Finkelmann, H. Liquid Crystal Elastomers: Influence of the Orientational Distribution of the Crosslinks on the Phase Behaviour and Reorientation Processes. *Macromol. Chem. Phys.* **1994**, *195* (4), 1353–1367. <https://doi.org/10.1002/macp.1994.021950419>.
- (44) Bastide, J.; Leibler, L.; Prost, J. Scattering by Deformed Swollen Gels: Butterfly Isointensity Patterns. *Macromolecules* **1990**, *23* (6), 1821–1825. <https://doi.org/10.1021/ma00208a044>.
- (45) Mendes, E.; Lindner, P.; Buzier, M.; Boué, F.; Bastide, J. Experimental Evidence for Inhomogeneous Swelling and Deformation in Statistical Gels. *Phys. Rev. Lett.* **1991**, *66* (12), 1595–1598. <https://doi.org/10.1103/PhysRevLett.66.1595>.
- (46) Onuki, A. Scattering from Deformed Swollen Gels with Heterogeneities. *J. Phys. II* **1992**, *2* (1), 45–61. <https://doi.org/10.1051/jp2:1992112>.
- (47) de Gennes, P. G. *Scaling Concepts in Polymer Physics*; Cornell University Press: Ithaca and London, 1979.
- (48) Huglin, M. B.; Yip, D. C. F. Microsyneresis Region in Poly(2-Hydroxyethyl Methacrylate) Hydrogels. *Macromolecules* **1992**, *25* (4), 1333–1337. <https://doi.org/10.1021/ma00030a020>.
- (49) Seiffert, S. Origin of Nanostructural Inhomogeneity in Polymer-Network Gels. *Polym. Chem.* **2017**, *8* (31), 4472–4487. <https://doi.org/10.1039/c7py01035d>.
- (50) Shiwaku, T.; Nakai, A.; Hasegawa, H.; Hashimoto, T. Ordered Structure of Thermotropic Liquid-Crystal Polymers. 1. Characterization of Liquid-Crystal Domain Texture. *Macromolecules* **1990**, *23* (6), 1590–1599. <https://doi.org/10.1021/ma00208a007>.
- (51) Chen, C. H.; Tang, C. W. Efficient Green Organic Light-Emitting Diodes with Sterically Hindered Coumarin Dopants. *Appl. Phys. Lett.* **2001**, *79* (22), 3711–3713. <https://doi.org/10.1063/1.1420583>.
- (52) Urayama, K.; Kohjiya, S. Crossover of the Concentration Dependence of Swelling and Elastic Properties for Polysiloxane Networks Crosslinked in Solution. *J. Chem. Phys.* **1996**, *104* (9), 3352–3359. <https://doi.org/10.1063/1.471018>.
- (53) Kumar, A. Calculation of Optical Parameters of Liquid Crystals. *Acta Phys. Pol. A* **2007**, *112* (6), 1213–1221. <https://doi.org/10.12693/APhysPolA.112.1213>.